



ELSEVIER

Contents lists available at ScienceDirect

Deep-Sea Research II

journal homepage: www.elsevier.com/locate/dsr2

Carlsberg Ridge and Mid-Atlantic Ridge: Comparison of slow spreading centre analogues

Bramley J. Murton^{a,*}, Peter A. Rona^b^a National Oceanography Centre, European Way, Southampton SO14 3ZH, UK^b Institute of Marine and Coastal Sciences, Rutgers University, New Brunswick, NJ 08901-8521, USA

ARTICLE INFO

Available online 29 April 2015

Keywords:

Mid-Ocean Ridge
Tectonics
Slow-spreading
Carlsberg Ridge

ABSTRACT

Eighty per cent of all mid-ocean spreading centres are slow. Using a mixture of global bathymetry data and ship-board multibeam echosounder data, we explore the morphology of global mid-ocean ridges and compare two slow spreading analogues: the Carlsberg Ridge in the north-west Indian Ocean between 57°E and 60°E, and the Kane to Atlantis super-segment of the Mid-Atlantic Ridge between 21°N and 31°N. At a global scale, mid-ocean spreading centres show an inverse correlation between segment length and spreading rate with segmentation frequency. Within this context, both the Mid-Atlantic Ridge super-segment and Carlsberg Ridge are similar: spreading at 22 and 26 mm/yr full rates respectively, being devoid of major transform faults, and being segmented by dextral, non-transform, second-order discontinuities. For these and other slow spreading ridges, we show that segmentation frequency varies inversely with flank height and ridge axis depth. Segments on both the Mid-Atlantic Ridge super-segment and Carlsberg Ridge range in aspect ratio (ridge flank height/axis width), depth and symmetry. Segments with high aspect ratios and deeper axial floors often have asymmetric rift flanks and are associated with indicators of lower degrees of melt flux. Segments with low aspect ratios have shallower axial floors, symmetric rift flanks, and evidence of robust melt supply. The relationship between segmentation, spreading rate, ridge depth and morphology, at both a global and local scale, is evidence that rates of melting of the underlying mantle and melt delivery to the crust play a significant role in determining the structure and morphology of slow spreading mid-ocean ridges.

© 2015 The Authors. Published by Elsevier Ltd. This is an open access article under the CC BY license (<http://creativecommons.org/licenses/by/4.0/>).

1. Introduction

1.1. Background

Slow spreading centres (spreading at a half-rate of less than 18 mm/yr) comprise 80% of the total length of the global mid-ocean ridge (MOR) system. Yet most of our knowledge of these types of spreading centre is derived from one type example, the central northern Mid-Atlantic Ridge, which is the best-known and most intensively studied slow spreading centre on Earth. This super-segment, between the Kane and Atlantis fracture zones (KAMAR), from 21°N to 31°N, has 100% multibeam bathymetry coverage and medium resolution sidescan sonar imagery (TOBI) along its ridge axis, numerous rock samples, and two well documented, high-temperature hydrothermal vent systems (the TAG and Broken Spur vent fields). In contrast, slow spreading centres from other ocean basins are less well known with possibly the

exception of the Reykjanes Ridge south of Iceland, a hot-spot affected oblique spreading centre that is anomalous in terms of depth, structure, tectonics and magmatism. Our knowledge of slow spreading centres elsewhere comes largely from incomplete multibeam bathymetry coverage, satellite and ship-derived gravity and derivative (predicted) bathymetry, some magnetic lines, sporadic rock-dredge sampling, and a few hydrothermal plume surveys. Despite this relative paucity of data, a number of general characteristic features are recognised for slow spreading centres.

Both fast and slow spreading mid-ocean ridges (MORs) are subdivided (Macdonald et al., 1988) into first-order segments, 10's to 100's km long, that are bound by active strike-slip transform faults that off-set the ridge axes by 10's of kilometres. Second-order segments further sub-divide first-order ones into short sections, a few 10's of kilometres in length that are bound by basins and non-transform discontinuities (NTDs) where the axis is displaced laterally by a few kilometres. These segments, that are characteristic of slow and ultra-slow spreading centres, have an axial valley of varying depth which hosts one or more volcanic centres defining a third-order segmentation (e.g., axial volcanic ridges). They also have a shallow central portion and deeper segment ends. Discontinuities that separate second-order segments along strike

* Corresponding author at: Ass. Head Marine Geosciences Group, National Oceanography Centre, University of Southampton Waterfront Campus, European Way, Southampton, SO14 3ZH, UK.

E-mail address: bjm@noc.ac.uk (B.J. Murton).

are often devoid of volcanic products and form fault-bounded short-wavelength sediment-filled basins, or horsts exposing lower crust and upper-mantle lithologies. Also, exclusive to slow and ultra-slow spreading centres are regions of axial asymmetry where one flank is significantly uplifted with respect to the other, and which often hosts a low-angle detachment fault exposing lower crust and upper-mantle lithologies in the footwall to form an oceanic core complex (OCC) (Tucholke et al., 1998; Cann et al., 1997). Off-axis trails of basins and highs can be traced back to current locations of on-axis NTDs and segment centres, indicating temporal continuity of the second-order segmentation process. In places, these trails form 'V'-shapes indicating migration of the loci of the segments with time (Rona, 1976; Rona and Gray, 1980; Schouten et al., 1987). Elsewhere, the off-axis morphological record shows second-order segments both merging and diverging and expanding and contracting in length (Tivey and Tucholke, 1998). The presence and evolution of such second-order segments have been attributed to spatial and temporal variations in magma supply, although the causes of these are poorly understood (Macdonald et al., 1988; Lin et al., 1990; Lin and Phipps Morgan, 1992; Cochran and Sempere, 1997; Magde and Sparks, 1997; Carbotte et al., 2004)

1.2. Aims and objectives

Here, we examine the relationships between second-order MOR segmentation, spreading rate, segment morphology, ridge depth and mantle melting for two slow spreading mid-ocean ridge analogues: the well known Kane to Atlantic super-segment (KA-MAR) of the Mid-Atlantic Ridge between 21°N and 31°N spreading at a half-rate of 11 mm/yr, and the lesser known Carlsberg Ridge (CR) in the north-west Indian Ocean between 57°E and 60°E, spreading at a half-rate of 13 mm/yr, (Fig. 1). These two MOR's are chosen because they have similar spreading rates, are distal from any hot-spot influence, and are located in two separate ocean basins: the Indian Ocean and the

Atlantic Ocean. The two spreading centres are placed in a global context by comparing them to other spreading centres using data taken from the Smith and Sandwell (1997) free-air gravity map, a recent compilation of global bathymetry, augmented by satellite altimetry (Becker et al., 2009), and plate tectonic models (DeMets et al., 2010). We then use multibeam bathymetry data to compare the morphology of the two slow spreading centre sections. The KA-MAR has extensive multibeam bathymetry coverage both on and off-axis, whereas the CR has limited multibeam coverage on axis, with off-axis bathymetry derived from the global bathymetry. A number of parameters that describe the morphology and tectonics of the spreading centres, including aspect ratio (flank height/axial width) and cross-section asymmetry, are examined and compared to geochemical attributes related to melt supply and mantle melting.

This contribution is not intended to be a synthesis of all work to date on the two ridges, although it draws broadly on that work to make comparisons. Instead, it is intended to define similarities and differences between the two slow spreading ocean ridges, to place them in a global context in order to stimulate insights into ridge processes, and to predict what may be discovered on the CR as exploration progresses in that remote area based on analogies with the Mid-Atlantic Ridge.

2. Methodology

2.1. Global MOR tectonics

The free-air gravity map was used to determine the broad tectonic characteristics and segmentation frequency of the major spreading centres around the world (Smith and Sandwell (1997)) (Fig. 1). For each MOR, the geographical location of the centre of each fracture zone (FZ), non-transform discontinuity (NTD) was identified, which in turn was used to define and record the centre,

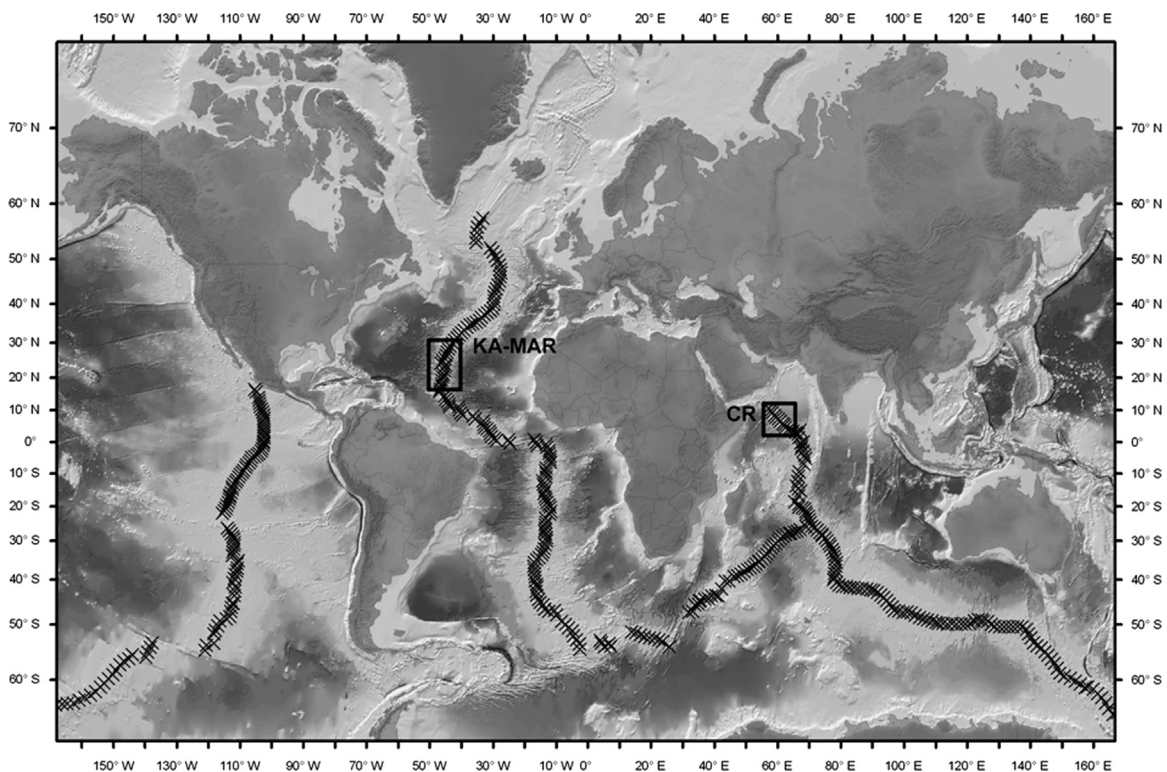


Fig. 1. Global bathymetry and topography showing the location of the Carlsberg Ridge (CR) and Kane to Atlantis super segment of the Mid-Atlantic Ridge (KA-MAR). Crosses show locations of the centres of second-order ridge segments for the major mid-ocean ridges and from which the segmentation parameters analysed in this contribution are derived.

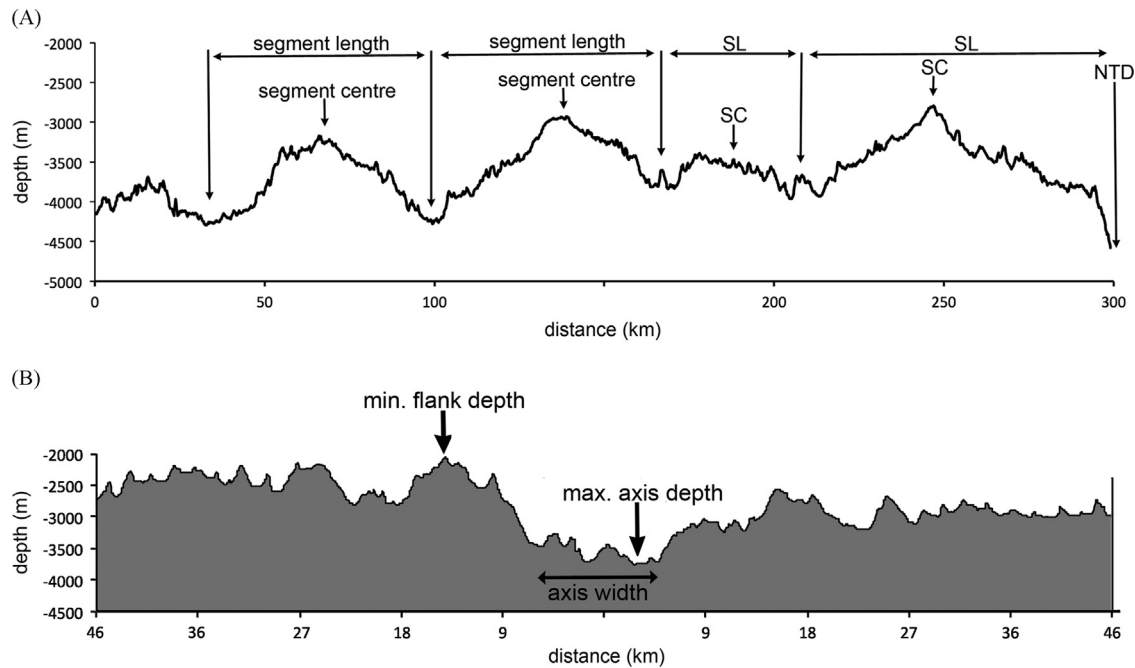


Fig. 2. Diagrams showing an example (from the CR) of how second-order ridge segment parameters are derived. (A) Along-axis bathymetric profile: segment length includes the distance to the centre of the bounding discontinuities; the segment centre is the shallowest point of each segment; and (B) Cross-axis bathymetric profile drawn parallel to the spreading direction and across the centre of a second-order segment from which the segment width is calculated as the distance between the foot of the scarps bounding the margins of the axial valley floor; and the maximum and minimum ridge depths are the deepest part of the axial valley and highest part of the rift flank, respectively.

length and orientation of the corresponding second-order ridge segments (Fig. 2). The segmentation frequency was calculated by summing the individual second-order ridge segments to give approximate windows to the nearest 500 km, and then normalised to an exact 500 km long window (while retaining the actual average segment length data) to allow comparison of segment frequency between different MORs.

Morphological features were identified and quantified from a gridded bathymetry data set (e.g. GEBCO 30" grid), which is based on satellite-derived gravity-predicted depth that is calibrated and constrained by actual ship-board soundings (Becker et al., 2009). Cross sectional profiles were drawn across the centres of the segments, and parallel to the direction of spreading (as indicated by the trend of transform traces), extending out to 5 Ma either side of the ridge (Fig. 1). Accordingly, cross sectional lengths vary with spreading rate (Table 1). From each profile, the ridge depth statistics (minimum, maximum and mean depth, plus standard deviation) were recorded and then averaged over the same 500 km long windows as used for the gravity data.

2.2. Local-scale MOR tectonics, morphology and geochemistry

Both the KA-MAR and CR have multibeam bathymetry coverage of their ridge axes. For the KA-MAR, these were collected by a *Sea Beam Classic* 12 kHz swath echosounder system during cruises RC2909 and RC2912 of the RV *Robert Conrad* in 1988 (Purdy et al., 1990) with additional data from cruises EW9212 and EW9607 of the RV *Maurice Ewing* in 1992 and 1996 (Table 2). These compiled and 100 m-gridded data were obtained from the National Geophysical Data Center, Boulder. Our CR multibeam bathymetry data were acquired using a SIMRAD EM12 12KHz multibeam echosounder during cruise CD149 of the RRS *Charles Darwin* in 2003 (Murton and Taylor, 2003; Murton et al., 2006) and were gridded at 100 m. Both bathymetry data sets extend to at least 6 km to each side of the ridge axis and capture the axial valley, inner rift

Table 1

Lengths of bathymetric profiles along spreading flow lines, out to 5 Ma to each side of the ridge axis, for different full spreading rates derived from the global bathymetry.

Ocean Basin	Lat./Long.	Full spreading rate (mm yr ⁻¹)	Profile length (km)
N. Atlantic	65°–50°N	23	115
	50°–30°N	25	125
	30°–0°N	26	130
S. Atlantic	0°–30°S	38	190
	30°–45°S	40	200
	45°–60°S	37	185
N., Central and SE. Indian	30°–10°N	18	90
	10°N–10°S	17	85
	10°–25°S	37	185
	25°–50°S	74	370
SW. Indian	70°–0°E	15	95
Pacific Ocean	145°E–135°W	66	330
	60°–50°S	88	440
	50°–35°S	99	495
(E. Pacific)	35°–10°S	185	925
	10°S–10°N	161	805
	10°–20°N	110	550
(Chile Rise)	70°–110°W	80	400

walls and the crests of the most proximal rift-valley flanks. The data are presented here as map and perspective images to illustrate the variety of morphologies present at both ridges. Cross-sections drawn parallel to the plate separation direction and across the centres of each of the second-order ridge segments are used to derive quantitative parameters describing the ridge morphology including maximum and minimum cross-section depth, flank height and axial valley width. Rock samples were also acquired from the CR during the same cruise.

Comparison is made between parameters describing the ridge morphology, along-axis depth, axial width, and basalt geochemistry (used as proxies for partial mantle melting). Major element

Table 2

Major element compositions of samples from the CR, analysed by XRF. Cr, Ni and V are expressed as ppm, the other oxides are expressed as weight-per cent.

Sample number	Latitude (+N)	Longitude (+E)	Depth (m)	SiO ₂	TiO ₂	Al ₂ O ₃	Fe ₂ O ₃	MnO	MgO	CaO	K ₂ O	Na ₂ O	P ₂ O ₅	Cr	Ni	V	total
CD149-WP4A D1	5.7487	61.4723	3743	51.1	1.3	14.7	10.4	0.2	7.5	11.6	0.28	2.7	0.13	347	258	111	99.80
CD149-WP4A D2	5.7487	61.4723	3743	50.5	1.6	14.8	11.1	0.2	7.3	11.1	0.25	2.7	0.16	350	274	82	99.77
CD149-WP6 D3	6.0517	60.9695	3578	50.9	1.2	14.6	10.4	0.2	7.9	12.0	0.15	2.4	0.12	411	265	92	99.82
CD149-WP6 D6	6.0517	60.9695	3578	50.4	1.4	15.3	10.6	0.2	7.8	11.4	0.20	2.3	0.14	363	283	76	99.79
CD149-WP7 D1	6.3452	60.6018	2166	50.6	1.1	15.2	9.6	0.2	8.5	12.1	0.23	2.1	0.12	406	222	114	99.84
CD149-WP7 D1	6.3452	60.6018	2166	51.1	1.5	15.5	10.3	0.2	7.4	11.0	0.17	2.5	0.15	375	228	107	99.82
CD149-WP7 D3	6.3452	60.6018	2166	50.3	1.0	15.4	9.8	0.2	8.5	12.2	0.13	2.3	0.08	486	236	720	99.82
CD149-WP7 D4	6.3452	60.6018	2166	51.2	1.2	14.7	10.1	0.2	7.8	11.8	0.21	2.4	0.12	360	272	104	99.85
CD149-WP8 D1	6.6045	60.3460	3451	49.6	1.7	14.9	11.2	0.2	7.7	11.3	0.32	2.8	0.20	387	255	89	99.79
CD149-WP8 D2	6.6045	60.3460	3451	50.6	1.7	15.1	10.9	0.2	7.6	10.7	0.27	2.6	0.19	392	286	120	99.80
CD149-WP9 D2	7.0417	59.9508	2918	51.4	1.3	15.0	10.0	0.2	7.7	11.4	0.18	2.5	0.12	386	268	120	99.82
CD149-WP9 D3	7.0417	59.9508	2918	51.2	1.1	14.9	9.8	0.2	8.1	11.9	0.14	2.4	0.10	446	262	97	99.79
CD149-WP9 D5	7.0417	59.9508	2918	51.8	1.3	15.3	9.9	0.2	6.8	11.7	0.24	2.5	0.12	424	238	89	99.84
CD149-WP11 D2	7.8745	59.4773	2563	52.2	1.4	15.1	10.0	0.2	7.1	11.1	0.29	2.5	0.14	389	237	71	99.90
CD149-WP11 D3	7.8745	59.4773	2563	51.6	1.2	14.6	10.1	0.2	7.3	11.7	0.31	2.7	0.13	297	256	69	99.85
CD149-WP13 D3	8.2067	58.7595	3902	50.9	1.6	15.4	10.5	0.2	7.3	11.1	0.23	2.7	0.15	383	243	111	99.88
CD149-WP13 D4	8.2067	58.7595	3902	51.0	1.6	14.9	10.8	0.2	7.3	10.9	0.26	2.7	0.16	406	282	105	99.81
CD149-WP13 D5	8.2067	58.7595	3902	51.0	1.2	14.6	10.1	0.2	7.8	11.9	0.20	2.6	0.12	314	277	81	99.83
CD149-WP14 D2	8.3785	58.5720	3583	51.3	1.5	15.0	10.4	0.2	7.4	11.2	0.27	2.6	0.16	294	280	95	99.87
CD149-WP15 D5	8.3785	58.5720	2731	50.9	1.4	15.3	10.2	0.2	7.8	10.7	0.19	3.0	0.13	300	254	125	99.77
CD149-WP16 D1	9.1542	58.2823	3725	51.2	1.7	14.8	11.2	0.2	7.5	10.3	0.17	2.6	0.18	280	260	129	99.82
CD149-WP16 D2	9.1542	58.2823	3725	51.5	1.7	14.9	11.0	0.2	7.0	10.4	0.31	2.9	0.18	247	309	127	99.89
CD149-WP17 D1	9.7363	58.0295	3908	51.7	1.8	15.0	11.0	0.2	6.6	10.1	0.37	2.9	0.21	290	275	93	99.82
CD149-WP18 D2	9.9218	57.6405	4100	51.2	1.4	15.7	9.7	0.2	8.0	10.7	0.19	2.6	0.15	358	220	149	99.78
CD149-WP18 D4	9.9218	57.6405	4100	51.0	1.4	15.8	9.6	0.2	8.0	10.8	0.26	2.8	0.15	320	192	152	99.85
CD149-WP19 D2	9.9705	57.0973	2664	50.9	1.4	15.2	10.4	0.2	7.8	10.8	0.13	2.8	0.13	291	249	128	99.79
CD149-WP19 D3	9.9705	57.0973	2664	50.9	1.5	15.1	10.5	0.2	7.7	10.7	0.16	2.9	0.14	286	230	113	99.80
CD149-WP19 D4	9.9705	57.0973	2664	50.3	1.4	15.1	10.3	0.2	8.0	11.2	0.17	3.0	0.13	287	253	135	99.83

geochemistry for the CR, reported here, was obtained from fresh, largely aphyric, whole rocks following removal of all alteration products, crushing, grinding and fusion with a lithium metaborate flux before analysis by wavelength dispersive X-Ray Fluorescence. Geochemical data for the KA-MAR is from the global geochemical compilation of Gale et al. (2014).

3. Results

3.1. Global MOR segmentation and tectonics

Analysis of second order segmentation frequency (normalised over 500 km-long windows) for the world's MORs reveals an inverse relationship ($R^2=0.45$) between segmentation frequency and spreading rate (Fig. 3A). Slow spreading centres, such as the Mid-Atlantic Ridge spreading at ~ 26 mm/yr, have significantly higher ridge segmentation frequency (6 segments/500 km) than faster spreading ridges, such as the East Pacific Rise (spreading at ~ 180 mm/yr and with a segmentation frequency of 4 segments/500 km). The analysis comprises data for 540 individual ridge segments, averaged and binned into 500 km long sections of the global MOR's. At the slow spreading end, the Reykjanes Ridge (RR) is anomalous by having a low-segmentation frequency that is more characteristic of the fastest spreading centres, possibly due to its location near, and influence from, the major ridge-centred hotspot forming Iceland (Murton and Parson, 1993; Searle et al., 1998; Murton et al., 2002). The northern Mid-Atlantic Ridge, near the Charlie Gibbs fracture zone, and the Chile Rise both have anomalously high segmentation frequencies (11 and 10 per 500 km) for their spreading rates (25 and 80 mm/yr, respectively); the northern Mid-Atlantic Ridge possibly resulting from its proximity to a major large-offset and double-stranded fracture zone (The Charlie Gibbs fracture zone) and being at the convergence zone between two mantle plumes (Iceland and Azores) (Schilling et al., 1983); and the Chile Rise from its proximity to an active subduction zone (the Chile Trench). Despite being in two different

ocean basins, the KA-MAR and CR have similar segmentation frequencies of 9 and 7 per 500 km, for spreading rates of 26 and 22 mm/yr, respectively. Overall, the linear relationship predicts the range of segmentation frequencies that fall between 8 and 2.5 per 500 km for respective spreading rates of 14 to 185 mm/yr.

From the analysis of segmentation frequency related to spreading rate (Fig. 3A), slow spreading ridges tend to show a higher segmentation frequency than fast spreading ridges. In accordance with this, plots of average segment length against spreading rate (Fig. 3B) show that slow spreading ridges have shorter segments than fast spreading ridges. The relationship ($R^2=0.65$) predicts segment lengths to range from 67 km at spreading rates of 14 mm/yr, to 223 km at 185 mm/yr. Anomalies occur for parts of the northern Mid-Atlantic Ridge and Chile Rise (with below average segment lengths) and the Reykjanes Ridge with anomalously long segments (as discussed above). The KA-MAR region has an average segment length of 58 km, which is close to the average for the CR of 68 km.

At a global scale, the spreading centres fall into spreading-rate clusters determined by the relationship between segment length and segment frequency (Fig. 3C). Ultra-slow spreading ridges (< 20 mm per year) are characterised by short and high-frequency segments (< 50 km long, > 10 per 500 km); slow spreading ridges (between 20 and 40 mm/yr) have segments of between 50 and 100 km long, with a frequency of between 6 and 9 per 500 km; intermediate spreading ridges (between 40 and 80 mm/yr) have segments of between 100 and 160 km long, with a frequency of between 4 to 5 per 500 km; and fast spreading ridges (> 80 mm/yr) have segments longer than 160 km, with a segmentation frequency of less than 4 per 500 km. Analyses of the individual segment data also shows that, while there is considerable spread at slow spreading rates, the variability of ridge flanks bathymetry (i.e., ocean floor roughness) increases with decreasing spreading rate (Fig. 3D).

3.2. Slow spreading centre morphology

The global bathymetry data has been used to construct spreading-parallel bathymetric profiles, extending to 5 Ma to each

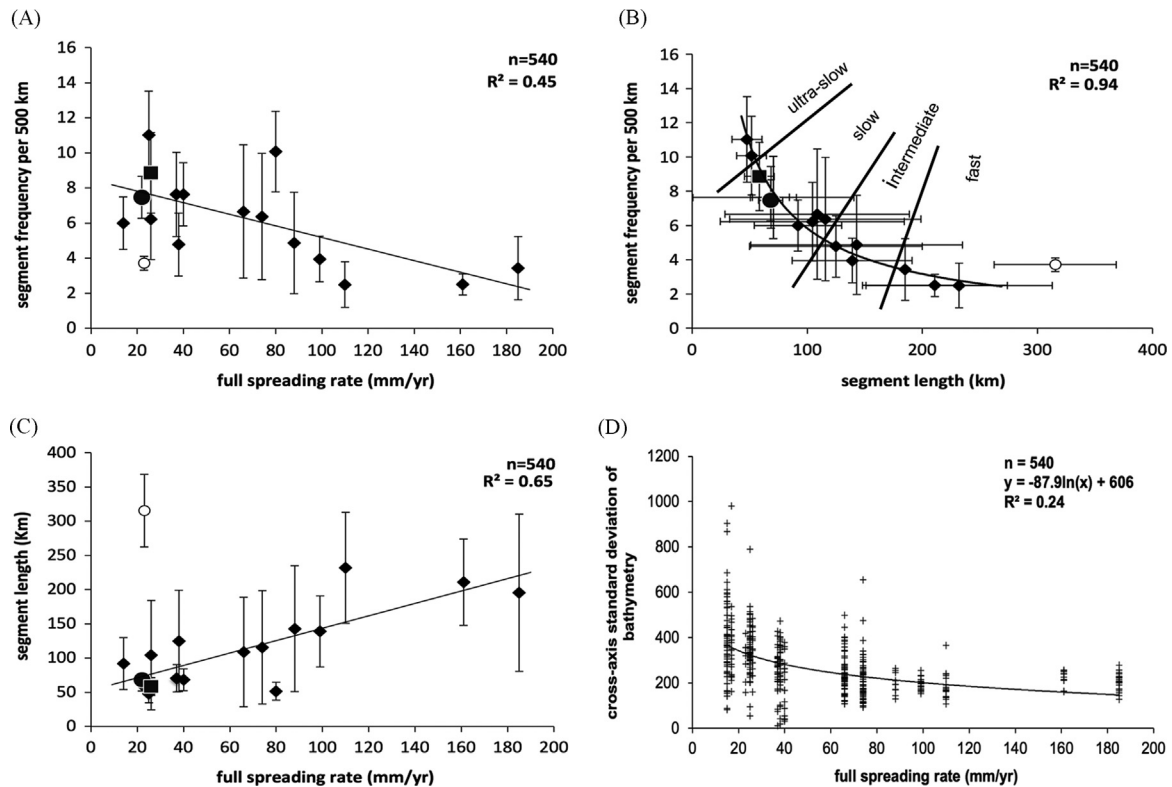


Fig. 3. (A) Global spreading rate vs. second-order segmentation frequency for 540, second-order ridge segments. Segment frequency is the average number of second-order segments for each of 500 km long spreading ridge sections and plotted against the prevailing spreading rates. Error bars denote the one-sigma standard deviation for each of the segment averages. Legend: filled black diamonds are the average number of second-order segments within a 500 km long window for a range spreading rates; open circle is the Reykjanes Ridge; filled black square is the KA-MAR; filled circle is the Carlsberg Ridge. (B) Global spreading rate vs. second-order segment length. Segment length is the average second-order segment length for each of 500 km long spreading ridge sections and plotted against the prevailing spreading rates. Legend as in (A) above. (C) Global segmentation frequency vs. second-order segment length. (D) MOR flank roughness (standard deviation of bathymetry for spreading-parallel cross sections) increases with decreasing spreading rate. Segment length and frequency, and their respective error bars, are calculated as for (A) and (B) above. Solid lines indicate partitioning between different full spreading rates: ultra-slow is less than 20 mm/yr, slow is between 20 and 40 mm/yr, intermediate between 40 and 80 mm/yr, and fast greater than 80 mm/yr. Legend as in (A) above. The R^2 value is calculated as the sum of the squares of the correlation coefficient between the actual data y_1 and those predicted by the best-fit function (f_1), and is expressed as, $R^2 = 1 - \frac{SS_{res}}{SS_{tot}}$, where $SS_{res} = \sum (y_1 - f_1)^2$, and $SS_{tot} = \sum (y_1 - \bar{y})^2$; f_1 is the best-fit function (e.g., in Fig. 2C, it is an exponential function with the form: $y = 339.03x^{-0.882}$); y_1 is the discrete data value; and QUOTE is the mean of the data.

side of the spreading centres, and located at the centre of each of the 540 second-order segments identified in this study. The profiles capture variations in the minimum depth of the rift flank shoulders, and the maximum depth of the axial valley floor, for each of the segments. As with the segmentation analysis, these data have been averaged and normalised to 500 km long windows.

Globally, the MOR data show no correlation between ridge flank elevation or axial floor depth and segmentation frequency (Figs. 4A and B). The global mean axial valley depth is 3520 m, and the average minimum rift flank depth is 2750 m. There are correlations, however, at an ocean-basin scale. Slow and ultra-slow spreading ridges (e.g., Mid-Atlantic Ridge and South-West Indian Ridge) show an inverse linear relationship between minimum rift flank depth and segmentation frequency such that high-frequency, short segments are associated with shallower rift flanks while low-frequency, longer segments correlate with deeper rift flanks. This relationship progressively inverts with increasing spreading rate such that intermediate spreading centres (e.g., South-East and Central Indian Ridges) show no correlation, and fast spreading centres (e.g., EPR) show a moderate increase in rift flank depth with increasing segment frequency (i.e., shorter segments have deeper rift flanks). The relationship between rift axis depth, flank elevation, and segmentation frequency is particularly well developed for the slow-spreading MAR such that short segments have deep axial valleys with shallow (uplifted) rift flanks. The KA-MAR and CR have rift flank depths of 2411 m and 2640 m and axial valley depths of

3608 m and 3706 m, respectively, which are typical for their segmentation frequency and slow-spreading rates.

3.3. Comparison between KA-MAR and CR general morphology

Within a global context, both the KA-MAR and CR are similar types of spreading centres: both are slow spreading and extend along strike for 900 km and 800 km, respectively, without interruption by major transform faults. They are both sub-divided by right-stepping non-transform discontinuities (NTDs), have similar second-order segmentation frequency, and similar depths for their ridge axes and ridge flanks (Fig. 5A and B). Along-axis profiles show thirteen second-order segments along the KA-MAR, and eleven along the CR (Fig. 6A and B). The spreading centres also show long-wavelength bathymetric variation across a depth range from 5000 m to 2500 m, with the KA-MAR becoming shallower to the north and the CR becoming deeper. NTDs at both spreading centres are marked by deep, short-wavelength basins. Elsewhere, other discontinuities are defined by narrow ridge-like features that cut obliquely across basins interrupting the spreading centre axis.

For the KA-MAR, many of the NTD's forming on-axis basins are associated with off-axis trails of basins forming troughs dissecting the flanks of the MOR, and which are oriented oblique to the spreading direction. These oblique, off-axis troughs are thought to be the fossil equivalents of the NTD basins, and their oblique-orientation to reflect the migration of temporally stable segments along the axis of the MOR (Sempéré et al., 1993). In places, the

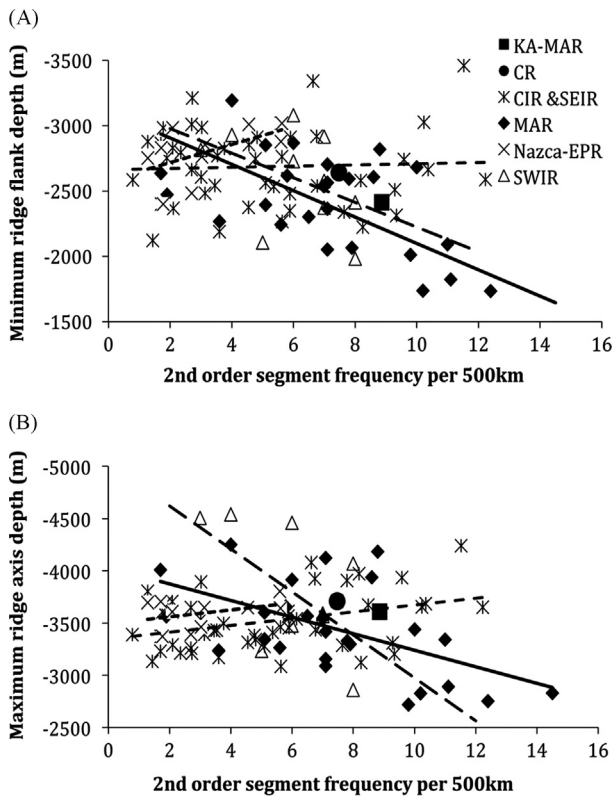


Fig. 4. (A) Global mid-ocean ridge flank depth vs. second-order segmentation frequency (per 500 km). The KA-MAR and CR have similar structure. For slow and ultra-slow spreading ridges (MAR and SWIR), segmentation frequency increases with decreasing (i.e., shallower) flank depth. Reverse holds for fast spreading ridges (Nazca and EPR). Legend: solid line is linear regression fit to Mid-Atlantic Ridge (MAR); long-dashed line fit to South-West Indian Ridge (SWIR); short-dashed line fit to Nazca and East Pacific Rise (EPR). (B) Global mid-ocean ridge axial floor depth vs. second order segmentation frequency (legend as in Fig. 4A above). For slow and ultra-slow spreading ridges, segmentation frequency increases with decreasing ridge axis depth. For intermediate and fast spreading ridges the converse holds.

off-axis troughs bound diamond-shaped regions of elevated ridge flank (e.g., KA-MAR segment 10) that indicate the waxing and waning of second-order segments along their length.

For the CR, the off-axis traces of the NTD's are less prominent (Fig. 5B). Where they are present, they are associated with short (< 10 km-long) oblique basins on the ridge axis (e.g., between segments 5 and 6, 8 and 9, 9 and 10) and follow a spreading-parallel orientation. Elsewhere, the NTDs are associated with either an asymmetric off-axis trace, appearing as a trough on one flank but not the other (e.g., segments 1–5 and 6 and 7) or are absent altogether. The presence of spreading-parallel traces indicates temporal stability of the segment-ends, bound by the larger NTD's, relative to their position along the spreading centre. For the remaining NTDs, their asymmetric or absent off-axis traces indicate more chaotic processes in which the relative positions of the segments are both temporally and spatially unstable, and the segments themselves are possibly episodic.

Across-axis bathymetric profiles for the KA-MAR and CR allow both the differentiation of common segment morphologies and comparison between the two ridges (Fig. 7). Contrary to previous work (Sempéré et al., 1993) in which the cross-axis profiles for the KA-MAR are described as either 'V' shaped or 'U' shaped, we recognize a spectrum of segment morphologies along the KA-MAR. These range from: 'V' shaped, where deep axial valley is deep and narrow (e.g., segment 5); to 'W' shaped, where an axial volcanic ridge (AVR) is present on the axial valley floor (e.g., segments 2 and 4); to segments that have raised and smooth axial floors forming an axial plateau or dome (segments 6, 9 and 10). A

further common morphology occurs where the rift flanks are deep and often asymmetric with one flank higher, smoother and more domed than its conjugate (e.g., segments 1, 2, 4 and 11). For the KA-MAR, deep and asymmetric segments predominate in the south, while smoother and flatter axial floors are more common towards the north.

For the CR, the distribution of segment morphologies is reversed: the proportion of segments with a shallow axial valley, and with domed, elevated and/or flat axial floors (e.g., segments 2, 3 and 6), is greater in the south, while in the north segments generally have deeper axial valleys and more asymmetric flanks (e.g., segments 9 and 11). These differences in segment morphology correspond to gross changes in long-wavelength MOR depth, with deep, wide axial valleys, often with asymmetric flanks, predominating where the MOR axis is deeper, and shallow narrow axial valleys, often with inflated axial domes and smooth axial floors, predominating where the MOR axis is shallower (Fig. 6C and D). While there is a relationship between along-axis segment amplitude (the difference in depth between the segment centre and its ends) and mantle Bouger anomaly for the northern MAR (Thibaud et al., 1998), we find no correlation between segment amplitude and axial depth, rift flank height, or cross-axis morphology for either the KA-MAR or CR.

3.4. Examples of common segment morphotypes

The common segment morphologies identified on both the KA-MAR and CR fall into three distinctive morphotypes: (1) symmetric segments with a shallow axial valley and smooth axial plateau; (2) symmetric segments with steep axial valley walls and a hummocky AVR; and (3) segments with a deep axial valley, with or without an AVR, and often with an anomalously elevated and asymmetric flank massif. For the KA-MAR, these morphotypes are typified by: segment 3 (flat wide axial floor), segment 6 (axial valley with a prominent AVR), and segment 4 (deep axial valley and asymmetric flanks) (Fig. 8A–C). For the CR, the corresponding segment morphotypes are typified by: segment 6 (smooth wide elevated axial plateau), segment 10 (wide axial valley and hummocky AVR), and segment 9 (elevated and asymmetric rift flanks) (Fig. 9A–C).

3.4.1. Symmetric segments with an elevated axial plateau or smooth seafloor and a wide axial valley

This type of second-order segment is characterised on the CR, for example, by the 50 km long segment 6 which has an 8.1 km wide, 660 m deep axial valley hosting an 11 km long axial dome or plateau. The flanks of the dome are smooth and dissected by a narrow graben. Each side of the dome, both smooth and flat-hummocky seafloor forms the axial valley floor and rift flanks. To the north, and especially to the south of the dome, a narrow hummocky-textured ridge forms a distinctive narrow and linear feature that extends to the ends of the segment. The rift flanks are characteristically regular with low (< 200 m), inward facing, linear fault scarps separating narrow (< 500 m wide) strips of seafloor. Segment CR 3 has a similar morphology with a 5.8 km wide, 600 m deep axial valley hosting a broad, smooth plateau.

A similar morphology characterises KA-MAR segment 3 where a 10.2 km wide, 1129 m deep axial valley is occupied by smooth and relatively flat seafloor that is domed at the segment centre, and which deepens towards the segment ends where it hosts narrow hummocky axial volcanic ridges. The rift flanks are regularly dissected by linear, inward facing, low (< 200 m) fault scarps that form a linear pattern of off-axis abyssal hills.

The texture of the seafloor at MORs is evidence for different volcanic eruptive histories (Griffiths and Fink, 1992a, 1992b): at CR segment 6, and KA-MAR segment 3, the smooth domed axial floor

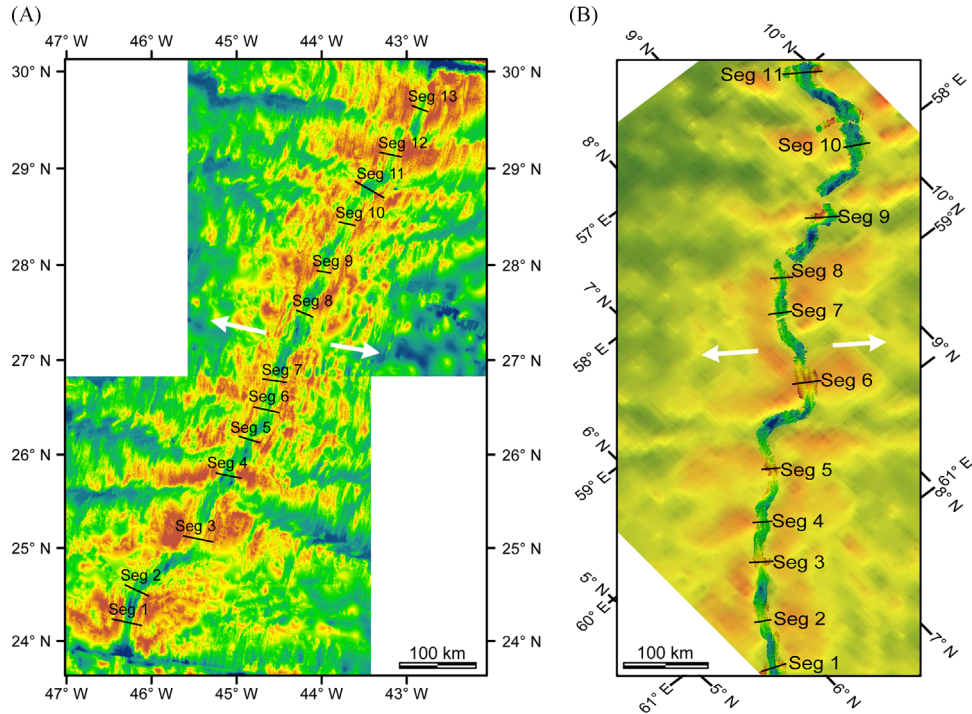


Fig. 5. Regional bathymetry displayed in histogram-normalised colour-coded shaded relief (red shallow, blue deep) for (A) the Kane-to Atlantis section of the Mid-Atlantic Ridge (KA-MAR), and (B) the northern section of the Carlsberg Ridge (CR), showing the available multibeam swath sonar bathymetry data (high-resolution) against a background of low-resolution predicted bathymetry (e.g. GEBCO). In (A), the KA-MAR, depths range from 2600 m to 5000 m, with a general shoaling of the MOR axis to the north. In (B), the CR, depths range from 1600 m to 5200 m, with a general northwestwardly deepening of the MOR axis. Both spreading centres are sub-divided into segments along their length by second-order discontinuities including non-transform discontinuities (NTDs). Segments are numbered consecutively from north to south and short black lines indicate profiles across segment centres. Both maps are displayed in a World Mercator projection; the CR map is rotated with respect to North for more effective presentation. Spreading directions (from DeMets et al., 2010) are shown by the white arrows. (For interpretation of the references to colour in this figure legend, the reader is referred to the web version of this article.)

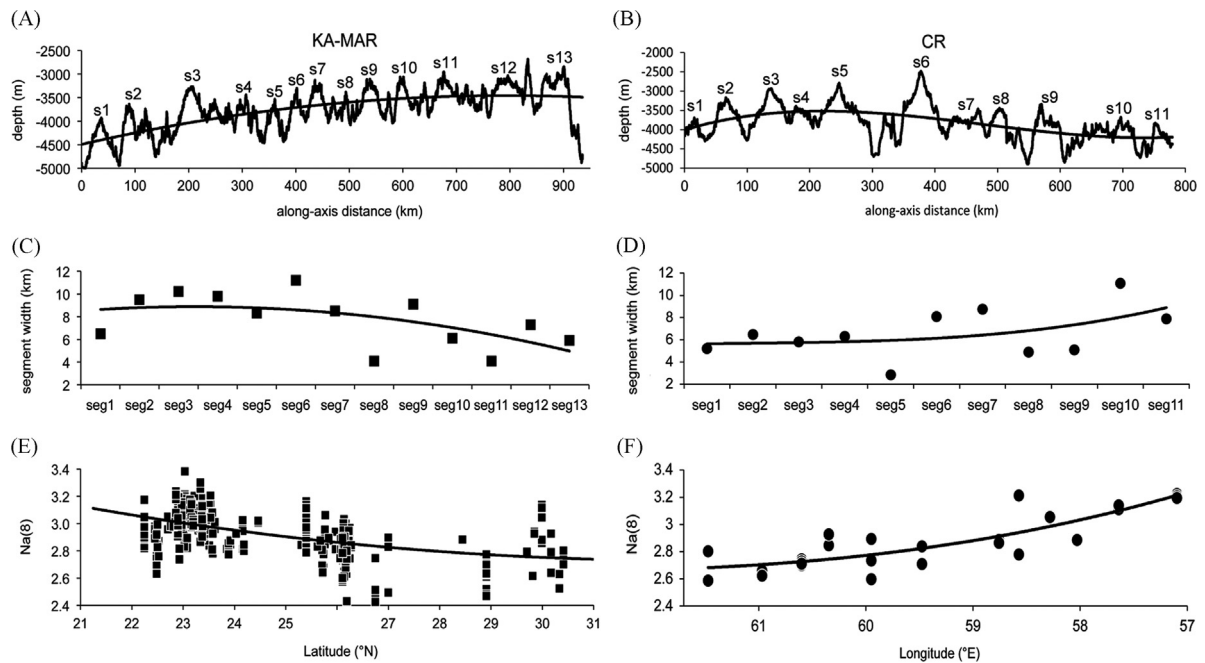


Fig. 6. (A, B): Along-axis bathymetry profiles for the CR and the KA-MAR showing second order segments (numbered) and 2nd order polynomial splines defining long-wavelength depth variations. In (A), the KA-MAR has 13 s-order segments that get progressively shallower over a distance northwards of ~900 km. In (B), the CR has 11 segments that get shallower and then deeper over a distance north-westwards of ~800 km. (B, C): Segment width, expressed as the distance between the innermost axial valley wall scarps at each segment centre, varies along the KA-MAR (C), and the CR (D), and with long-wavelength axial depth (A, B) such that narrow axial valleys occur where the ridge axes are shallower, and broader axial valleys where the ridge is deeper. (E, F): $Na_{(8)}$ is used as a proxy for the degree of partial melting of the sub-oceanic spreading centre mantle. Data for the KA-MAR is taken from the global compilation of mid-ocean ridge basalts by Gale et al. (2014) and uses their derivation of $Na_{(8)}$. Basalt geochemistry data for the CR is from this study and is based on whole-rock XRF analyses of fresh basaltic glassy whole rocks. The method used to compute $Na_{(8)}$ is derived from these samples using a least-squares linear regression of the correlation between Na_2O and MgO . For both the KA-MAR and CR, $Na_{(8)}$ shows a positive correlation with long-wavelength ridge depth and axial valley width (i.e., $Na_{(8)}$ increases with increasing ridge depth). Together this indicates a relationship between mantle melting ($Na_{(8)}$), mantle temperature (axial depth) and segment morphology.

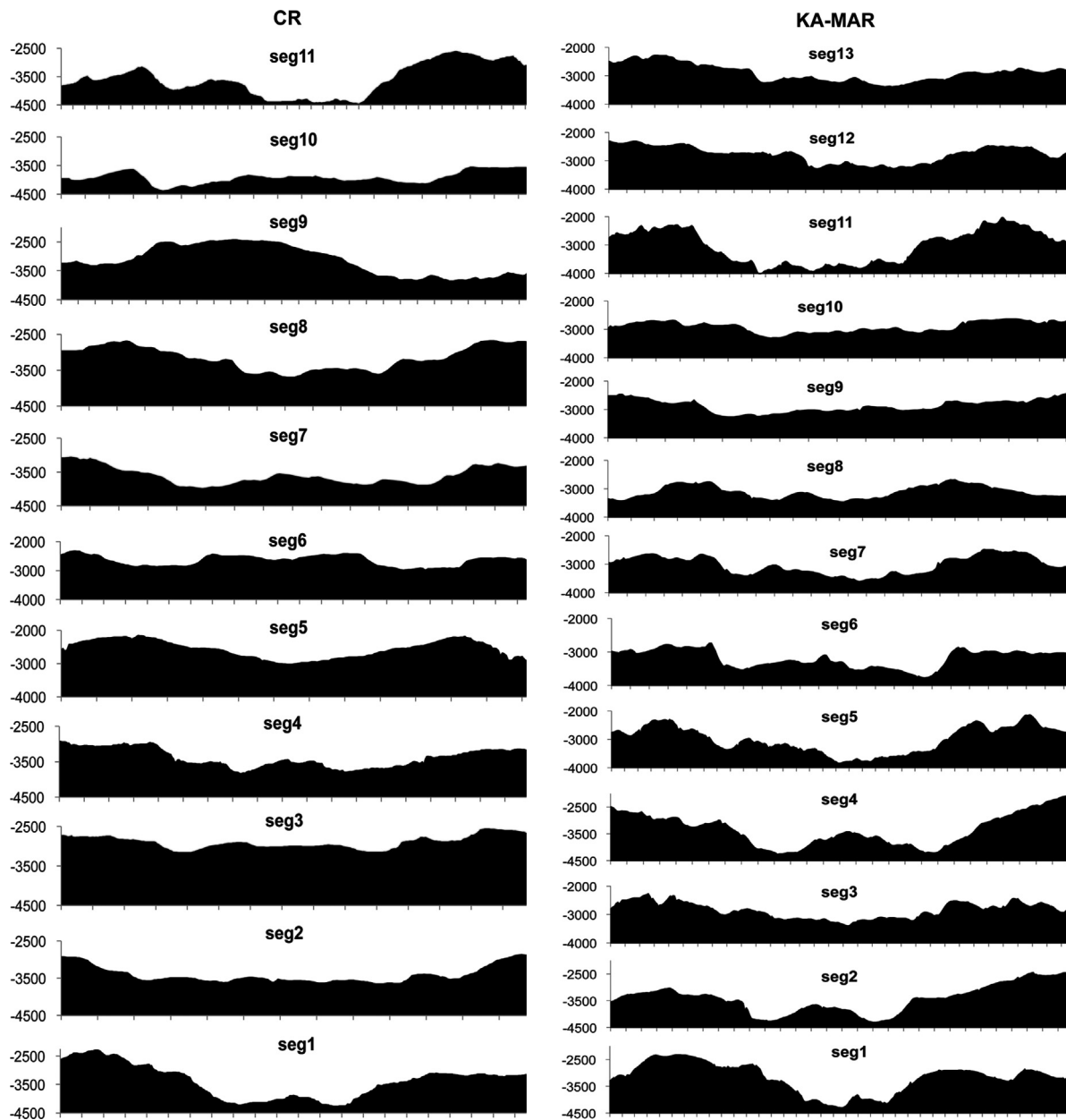


Fig. 7. Stacked bathymetric cross-sections from multibeam bathymetry data for the CR and KA-MAR drawn parallel to the plate spreading direction and across the centres of second-order segments. Segments are numbered consecutively from south to north. Vertical axes show depths in metres; horizontal axes show distance in kilometres (ticks). The cross-section profiles (except for CR segment 9) are centred on the ridge axes and are displayed at a variety of scales.

indicates rapid eruptions of relatively large volumes of lava. The closely spaced, low-throw fault scarps, and regular abyssal hills, and wide low-relief axial valleys, are also evidence of a thin, weak (and thermally warm) lithosphere for these segment morphotypes (Phipps Morgan et al., 1987; Buck et al., 2005). Spreading centre segments that show smooth and inflated morphologies, such as those here, are usually associated with relatively high melt flux such that a high proportion of plate separation is accommodated by volcanic activity and the accretion of magmatic crust (Sempéré et al., 1993; Hooft and Detrick, 1995; Gente et al., 1995).

3.4.2. Symmetric segments with steep axial valley walls and hummocky AVRs

This type of second-order segment is characterised on the CR by the 116 km long segment 10 (Fig. 9). Here, the ridge has an 11.1 km wide, 820 m deep axial valley, bound by steep (30–45°) fault scarps forming

axial valley walls, that is host to a broad and hummocky axial volcanic ridge of up to 40 km long and 450 m high. The AVR, which is parallel to the MOR axis, occupies up to 75% of the width of the axial valley floor. Some circular seamounts (< 500 m diameter) are aligned in rows along the crest and flanks of the AVR. Hummocky seafloor occupies the axial valley floor, which is bound by curvilinear and irregular rift walls comprising a series of inward and outward facing fault scarps up to 800 m high. The rift flanks include back-rotated fault-bounded blocks with outward dipping seafloor indicative of tectonic back-rotation. Segment 6 on the KA-MAR has similar morphology including a 1.2 km wide, 1092 m deep axial valley occupied by a broad, up to 300 m high, hummocky textured AVR that deepens towards the segment ends (Fig. 8). The axial valley is bound by up to 500 m high, steep (35–45°) and inward-facing fault scarps. The rift flanks are dissected by irregular-shaped, curvilinear, inward facing, < 300 m high scarps bounding steeply back-rotated (by up to 12°) fault blocks that form a distinctive pattern of irregular off-axis abyssal hills.

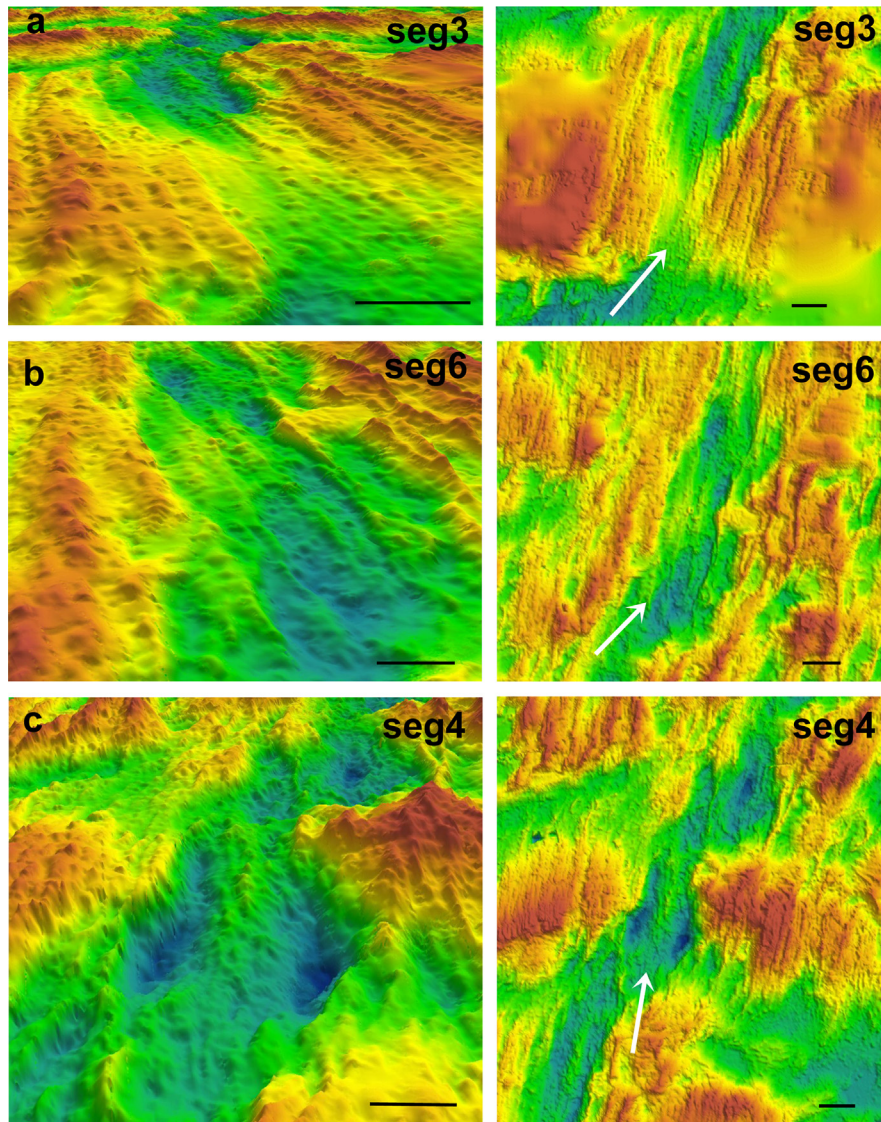


Fig. 8. Detailed bathymetry (right—North to the top) and 3D perspective views (left—with 2x vertical exaggeration) of second-order segment morpho-types along the KAMAR (see Fig. 5A for locations). Black scale bar represent a length of 5 km. The white arrow indicates the direction of look for the perspective views. Depth-indicated colours are the same as those in Fig. 5A: (A) segment 3 displays a smooth axial floor and low rift flanks; (B) segment 6 has a hummocky and deeper axial valley with a topographically subdued axial volcanic ridge; (C) segment 4 has a deep and asymmetric axial valley, elevated flanks, a topographically prominent axial volcanic ridge. (For interpretation of the references to colour in this figure legend, the reader is referred to the web version of this article.)

The presence of an AVR is typical for most slow spreading ridges. An examination of the available multibeam bathymetry data sets for slow spreading MORs (e.g., www.ngdc.noaa.gov/mgg/bathymetry/multibeam) reveals ~75% of all slow spreading, second order, MOR segments have AVR's (the remainder being either volcanically inflated and domed segments or occupied by deep basins). While there remains some uncertainty as to whether they are the product of episodic or continuous magmatic processes (Head et al., 1996; Mendel et al., 2003), the origin of AVR's is clearly magmatic. The presence of a moderately deep axial valley floor and sharply defined, steep rift walls may be the result of magmatic subsidence beneath the axial valley floor, while the back rotation of fault blocks on the rift flanks indicates a significant contribution to plate separation that is also made by tectonic stretching (Buck et al. 2005).

3.4.3. Segments with a deep axial valley with or without an AVR, often with an anomalously elevated asymmetric flank massif

At the CR, this type of segment is characterised by segment 9 (Fig. 9). Here, the ridge is offset to the north-east by a right-lateral

NTD. The 60 km long segment has a relatively narrow (5.1 km wide) and deep (1427 m) axial valley, with a hummocky textured axial floor containing a number of circular (~1 km diameter) seamounts and linear ridges. A 15 km wide, 20 km long, 1400 m high massif dominates the south-western flank of the ridge segment. This feature (named here as 'Raourkes Drift') has a smooth, domed surface, ornamented by prominent spreading-parallel corrugations. Its margin closest to the ridge axis dips at 22° towards the spreading centre, and is close to the contact with the hummocky neo-volcanic terrain of the axial valley floor (Fig. 10A). The smooth, corrugated and domed surface of the massif exposes assemblages comprising mylonites, amphibolites, gabbros and peridotites (Fig. 10B–C). Here, mylonitic amphibolites are cross-cut by micro-granitic veins indicating high-temperature deformation (at amphibolite-facies conditions) and melt invasion from either late-stage mafic melts or mafic crustal melts both during and after deformation. The morphology, texture, surface corrugations, and petrology of Raourkes Drift are all characteristic of the footwall of oceanic core complexes, where low angle detachment faults exhume deformed and metamorphosed rocks that are typical of the lower oceanic crust and upper mantle (Tucholke and Lin, 1994; Tucholke

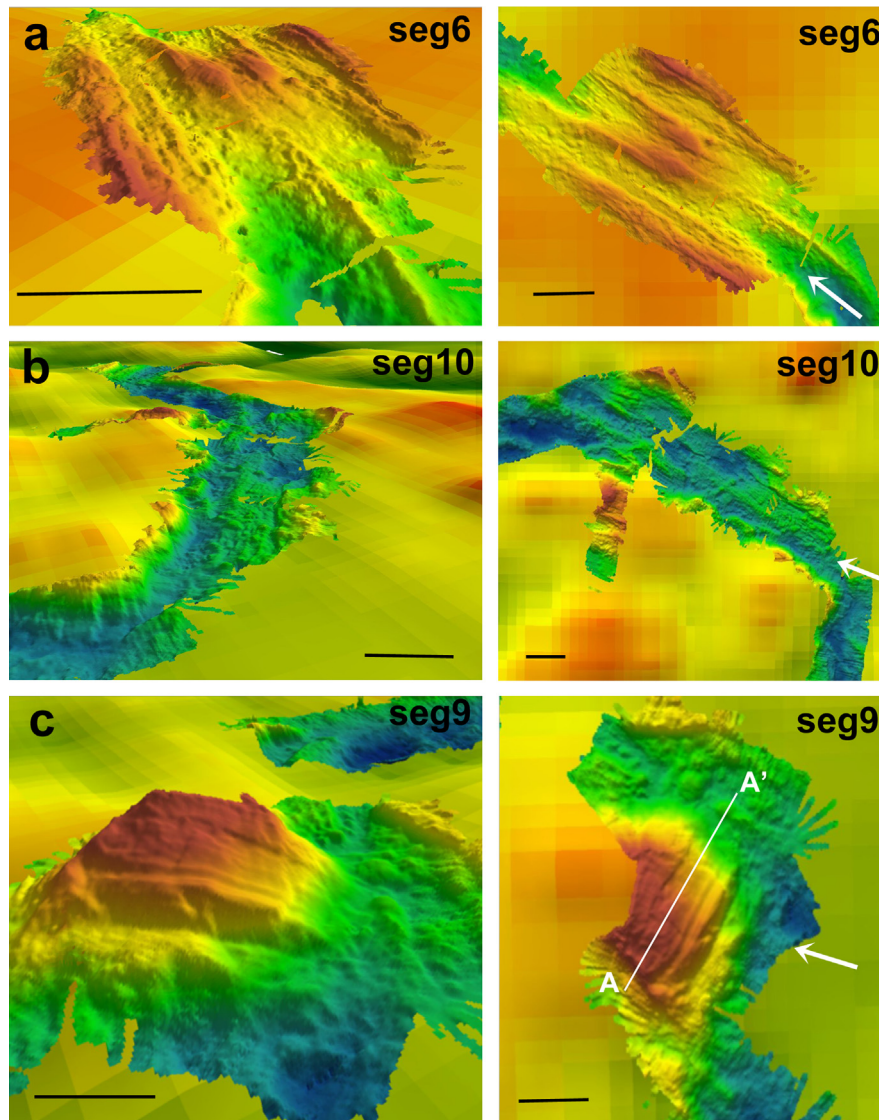


Fig. 9. Detailed bathymetry (right—North to the top) and 3D perspective views (left—with 2x vertical exaggeration) of second-order segment morpho-types along the CR (see Fig. 5B for locations). Black scale bar represent a length of 5 km. The white arrow indicates the direction of look for the perspective views. Line A–A' marks the cross-section, shown in Fig. 10A. Depth-indicated colours are the same as those in Fig. 5B: (A) segment 6 displays a smooth axial floor dome, a narrow AVR, and topographically low rift flanks; (B) segment 10 shows topographically elevated rift walls, a hummocky axial floor, and a hummocky axial volcanic ridge; (C) segment 9 shows a deep and asymmetric axial valley with a hummocky axial floor and a smooth, domed, topographically elevated axial massif to the west with NE-SW oriented corrugations. (For interpretation of the references to colour in this figure legend, the reader is referred to the web version of this article.)

et al., 1998; Cann et al., 1997). The ductile shear fabrics and granitic veins are possibly the result of the close proximity of the termination zone of the *Raourkes Drift* oceanic core complex to the zone of active magmatism, resulting in high-temperature deformation condition for the detachment fault beneath the hanging wall of the axial valley.

While there are no corrugated massifs at the KA-MAR, segment 4 is 9.8 km wide, has a 2197 m deep axial valley, and has a prominent massif forming its eastern ridge flank (Fig. 8C). While there is no obvious low-angle detachment fault forming this massif, it rises to over 2200 m from the axial valley floor, forming an asymmetric eastern flank to the centre of the ridge segment. The axial valley at this location also contains a prominent 650 m high, 34 km long, hummocky textured AVR with an orientation that is slightly (12°) oblique to the strike of the spreading axis. Elsewhere along the KA-MAR, segments 1 and 11 also have deep (> 2000 m) axial valleys that range from 6.5 to 11.2 km wide, with elevated and often domed massifs on their ridge flanks. Segment 1, for example, contains a small (250 m high, 30 km long) AVR, while segment 11 has a relatively flat and tectonised axial valley floor.

Deep and asymmetric segments, and those containing oceanic core complexes, have been ascribed to low magma flux and increased accommodation of plate separation by tectonic deformation, deep sub-moho emplacement of magmas, and the development of long-lived, low-angle, normal (detachment) faults (Cann et al., 1997; Lavier et al., 1999; Ildefonso et al., 2007; MacLeod et al., 2009; Olive et al., 2010). On this basis, those segments at the CR and KA-MAR that exhibit flank asymmetry and OCC formation, deep axial valleys, with or without axial volcanic ridges, and with generally wide axial valleys at their segment centres, are likewise considered to reflect low magma supply and the dominance of tectonic stretching accommodating seafloor spreading.

4. Discussion

The variations in segment morphology described above can be quantified from the segment centre profile data describing the minimum depth of the rift flank, maximum depth of the axial

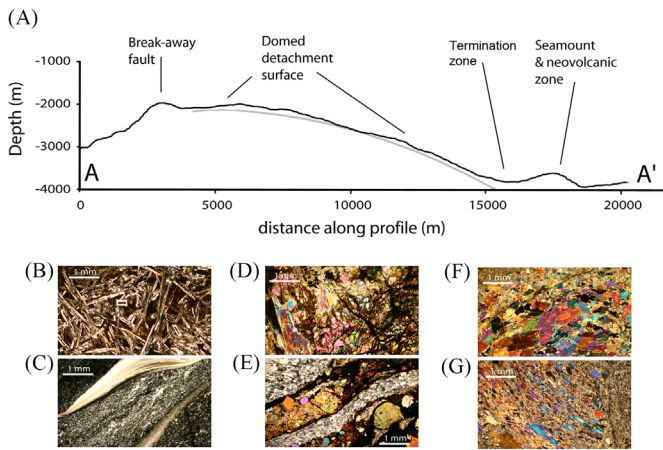


Fig. 10. (A) Bathymetric section (derived from EM12 multibeam bathymetry data gridded at 100 m) across the corrugated massif *Raourkes Drift* (see Fig. 9C, section A–A' for location). The profile (black line) shows a domed detachment surface that has an increasing dip (grey line) with increasing depth (from 1.5° to 22°). The foot of this slope marks the boundary (or termination zone) between the domed foot-wall (detachment fault surface) and the young volcanic zone of the axial valley floor (forming the hanging wall). The western-most end (left) of the profile is marked by a NW–SE ridge and steep west-facing hummocky slope forming the break-away zone, marking the start of the detachment fault surface. Photomicrograph of rocks collected by dredges across the massif in order from east to west (white scale bar represents 1 mm): (B) High-Mg spillitic lava from the volcanic zone of the hanging wall; (C) Sheared serpentinite and talc schist; (C) Cataclastic peridotite (harzburgite), (E) Mylonitic olivine gabbro overprinted by neoblastic felsic (granitic) veins, (F) Mylonitic amphibolite after gabbro, and (G) Mylonitic olivine gabbro.

valley floor, and axial valley width. For both the KA-MAR and CR, the relationship between segment-profile aspect ratio partitions the observed segment morphology into magmatically and tectonically dominated seafloor spreading (Fig. 11A). Segment centres with elevated rift flanks for a given axial width tend to be tectonically dominated (e.g., segments Cs11, Cs9, Ks1 and Ks11), whereas those with low axial flanks for a given axial width are more magmatic (e.g., segments Cs3, Cs6, Ks9 and Ks10). Since the axial width of a segment at its centre can vary significantly for either magmatic or tectonic segment types, the ratio between flank height and axis width is used here to define a segment centre aspect ratio which accommodated this variability such that low aspect ratios identify those segments dominated by magmatic spreading, and high aspect ratios identify ones dominated by tectonic spreading.

Further discrimination between segment morphotypes can be realised through plotting segment centre aspect ratios against flank heights (Fig. 11B). For both the CR and KA-MAR, the data define broadly linear trends in which those segments that have both a high aspect ratio and high flank heights (i.e., tectonic segments) are distinguished from those that have low aspect ratios and low flank heights (i.e., magmatic). Further analysis reveals a broadly linear relationship between the actual depth below sea level of the ridge axis at the segment centre (i.e., maximum depth of the axial valley floor) and the maximum height above the axial floor of the adjacent flank (Fig. 11C). This identifies a spectrum of segment morphologies from those with a shallow axial floor and low flank height (i.e., magmatically robust); those that are intermediate (i.e., characterised by an AVR); and those with deep axial floors and high flanks (i.e., tectonic). This analysis also identifies segment 1 on the CR (i.e., Cs1) as being dominated by tectonic spreading. While the segment morphology reveals asymmetric flanks and a deep axial valley floor, it also hosts a robust AVR, and the elevated (south-western) flank does not show any evidence for corrugations or low-angle detachment faulting. This raises the possibility that oceanic core complex formation is not the only

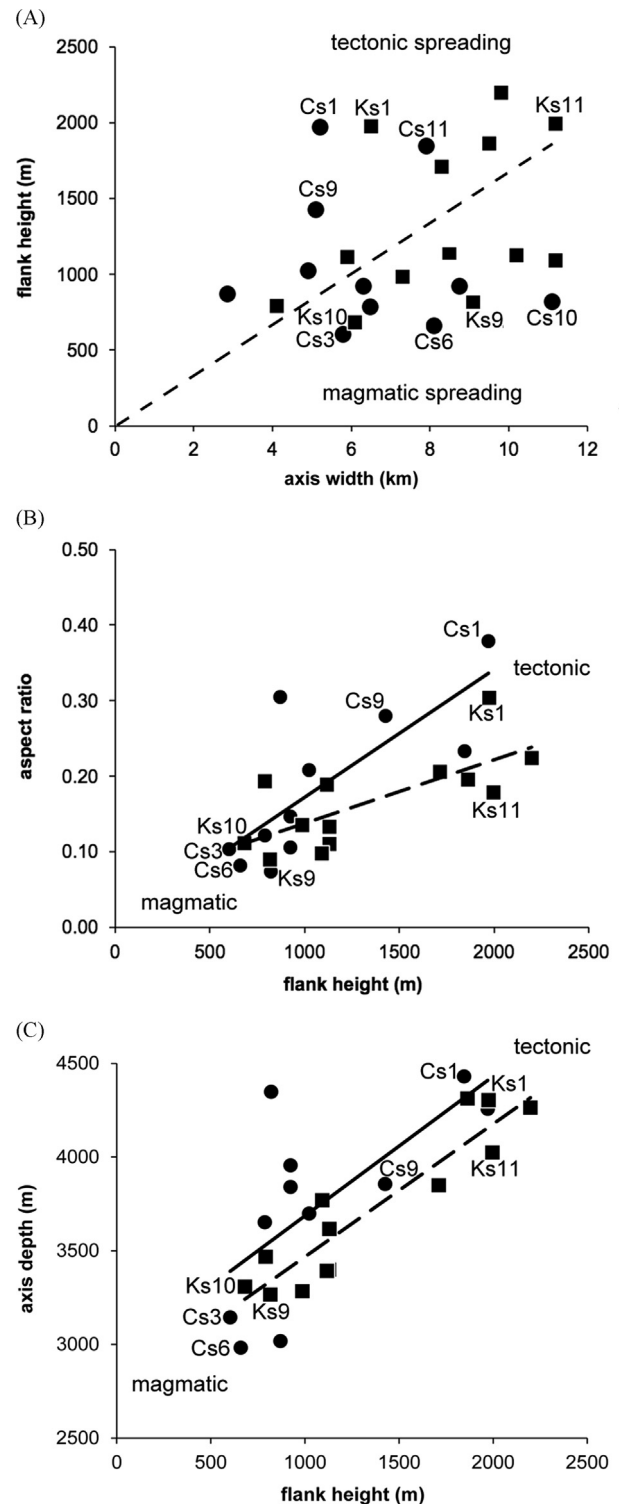


Fig. 11. Diagrams showing relationships between second-order ridge segment morphological characteristics for the CR and KA-MAR. Legend: filled circles are CR segments (individual examples are prefixed Cs), and those the KA-MAR are filled squares (individual examples are prefixed Ks). Segment numbers refer to bathymetry profiles in Figs. 5 and 7: (A) Rift flank height vs. axial width showing those segments with high rift flanks and narrow segment axes are generally characterised by tectonic spreading styles, and those with shallow rift flanks and broader segment axes are generally characterised by magmatic spreading styles. (B) Segment aspect ratio vs. flank height discriminates magmatic segments (low aspect ratio, subdued flanks) from tectonic ones (high aspect ratio, elevated flanks). (C) Segment axis depth vs. flank height shows that those segments with elevated rift flanks also have deeper spreading axes and are characteristically tectonic in style, whereas segments with subdued flanks and shallow spreading axes are more magmatic.

morphological manifestation of low melt supply to slow spreading centres. In addition, large throw, multiple faults resulting in uplifted flanks can also accommodate plate separation without the need for low angle detachment faults.

Comparison between the CR and KA-MAR shows that the KA-MAR segments have consistently lower aspect ratios for given flank heights, and have shallower (by 180 m) axial valley floors (Fig. 11A–C). Both the CR and KA-MAR have predominately magmatic segments, although the KA-MAR also has more of a bi-modal distribution in segment morphology, grouping into either tectonic or magmatic dominated spreading.

There are several hypotheses for the origin of deep axial valleys ranging from temperature-controlled viscosity of the asthenosphere (Osmaston, 1971) to models showing that the axial structure of MORs is very sensitive to the thermal structure of the oceanic lithosphere as a result of different spreading rates and axial cooling by hydrothermal circulation (Phipps Morgan et al., 1987; Chen and Morgan, 1990). For slow and intermediate spreading rates, such models also predict that the width and depth of axial rift valleys decrease with an increase in either the thickness of the oceanic crust or higher mantle temperature (i.e., a thicker crust and/or hotter mantle temperatures produce a less pronounced rift valley) (Hooft and Detrick, 1995). The dependency of slow spreading MOR axial morphology on local magmatic input is also predicted by finite element models (Buck et al., 2005), where plate stretching and differing amounts of axial magmatic intrusion dominate changes in axial fault styles. In these models, slow spreading MORs, with a magmatic to tectonic spreading ratio (M) of 0.95 (i.e. magmatic-dominated spreading), generates symmetric rift flanks with a shallow axial valley. Conversely, $M \leq 0.5$ generates asymmetric MORs with a deep axial valley with increasingly large offset normal faults uplifting flank massifs exposing lower crust and upper mantle lithologies.

Our analysis largely supports the predictions of these models. For both the CR and KA-MAR, the height of the flanks correlates strongly with the depth of the axial valley floor. This is not the case for axial widths. Although axial width is quite variable, at a longer wavelength we find the width of the axial valley broadly correlates inversely with long-wavelength variation in along-axis depth (Fig. 6A–D). Both the CR and KA-MAR, where the ridge axis is deep and segments are more likely to be asymmetric with a broad and often deep axial valley, have a high aspect ratio, and are dominated by tectonic spreading. Where the ridge is shallow, the segments are commonly symmetric with a shallow, smooth, domed and often narrow axial valley floor, a low aspect ratio and to be dominated by magmatic spreading. At a segment-scale, these changes may reflect both the local and transient magmatic input as well as the longer thermal structure of the mantle and lithosphere, including the magma flux.

Our analysis shows relationships between spreading rate, ridge depth and segmentation frequency at an individual spreading ridge scale. For the global MORs, a decrease in second-order segmentation frequency and increase in segment length is consistent with a thermal and tectonic origin for the segments such that at fast spreading rates, with high magmatic flux, the ridge axis has a hot thermal structure and a weak lithosphere (Thibaud et al. 1998, 1999; Rabain et al., 2001). As a result, the location of the ridge axis is plastic and subtle differences in spreading rate, rift orientation and magma flux are accommodated by bends and lateral migration of a continuous accretionary zone. In this view, intermediate and fast spreading ridges can be considered quasi-continuous magmatic rifts, punctuated by gaps in magma supply, resulting in tectonic discontinuities (NTDs). This also holds for hot-spot affected MORs such as the Reykjanes Ridge south of Iceland. In contrast, slow spreading rates result in cooler and hence stronger lithosphere at the ridge axis and flanks, with a correspondingly more rigid behaviour of the accretionary zone. Here,

changes in magma flux result in punctuated melt focusing, with strain partitioned between segments with the different tectonic styles and accommodated by lateral displacement and shear across NTDs.

For the KA-MAR and CR, where differences in spreading rate are not significant, the relationship between segmentation frequency, segment length and ridge depth indicate that local magma flux has a strong influence on ridge morphology. Where the axial valley floor is relatively shallow, and the axial flanks are low (i.e. typical of a magmatic segment), segmentation frequency is high and the segments are short. This observation can be explained, for slow-spreading MORs, where a relatively high magma supply is strongly three-dimensional with multiple loci of melt delivery, each generating their own magmatic segment. Where magma supply is low, tectonic spreading dominates by the linking of large throw normal faults accommodating along-axis changes in strain, resulting in longer ridge segments. In this alternative view, slow spreading centres form a quasi-continuous, stretching-dominated rift system that is punctuated by a spatially discontinuous supply of melt such that the centres of magmatic accretion form the ridge axis discontinuities. Hence, the supply of melt dominates not just the segment morphology, but also the segmentation frequency.

Globally, the relationship between axial depth and mantle melting (and hence melt supply) has been explored using major element proxies for mantle melt fraction, especially for spreading centres distal from mantle heterogeneities including hotspots (Klein and Langmuir, 1987; Gale et al., 2014). The use of sodium concentrations corrected for fractional crystallisation (i.e. Na and to 8 wt% MgO , termed $Na_{(8)}$) is used here to indicate the degree of mantle melting along the CR. At a long-wavelength scale, $Na_{(8)}$ inversely correlates with axial depth (Fig. 6E,F) indicating a decrease in melt fraction north-west along the CR, as the mean long-wavelength depth increases. This indicator of mantle melt fraction is a qualitative proxy for melt flux and the mean long-wavelength ridge depth is an indicator of mantle temperature. Hence, the CR appears to progressively decrease in both melt flux and mantle temperature towards the northwest, and its intersection with the Owen fracture zone.

Assuming the oceanic crust generated at these two spreading centres is formed by isentropic decompression of passively upwelling anhydrous MORB mantle (McKenzie and Bickle, 1988), an empirical estimate of the variation in mantle potential temperature can be derived from the long-wavelength variation in depth of the water-loaded, zero-age, axial crust (Klein and Langmuir, 1987; White et al., 1995). For this, we used Eq. (1), adapted from White et al. (1995) and Poore et al. (2009):

$$\Delta T_p \approx K \left[\left(\frac{\rho_a - \rho_w}{\rho_a - \rho_c} \right) (dr_1 - dr_2) \right] \quad (1)$$

where ΔT_p is the difference in mantle potential temperature ($^{\circ}C$), ρ_a is the density of asthenospheric mantle ($3.2 \times 10^6 \text{ g m}^{-3}$), ρ_c is the density of oceanic crust ($2.8 \times 10^6 \text{ g m}^{-3}$), ρ_w is the density of seawater ($1.0 \times 10^6 \text{ g m}^{-3}$), and dr_1 and dr_2 are the maximum and minimum long-wavelength, water-loaded, axial depths (km), and K is an empirically derived scaling factor between mantle temperature and axial depth ($16 \text{ }^{\circ}C/km$).

This treatment yields an approximation of the change in mantle potential temperature for a given change in median axial valley depth. While the values may not be absolute, the relative differences yield an indication of the magnitude of temperature variation along each MOR. For the CR, the long-wavelength axial depth varies from 3500 m to 4200 m, which corresponds to a variation in mantle potential temperature of $\sim 61 \text{ }^{\circ}C$ or $0.08 \text{ }^{\circ}C/km$ (i.e., a change of between 4.7% and 4.9%, assuming a minimum T_p of between 1250–1300 $^{\circ}C$). The long-wavelength axial depth variation along the KA-MAR is slightly greater, varying from 3450 m to 4400 m, corresponding to a variation in mantle

potential temperature of $\sim 83^\circ\text{C}$ or $0.09^\circ\text{C}/\text{km}$ (i.e., a change of 6.2% to 6.5%).

The changes in second-order ridge segment morphology: aspect ratio, ridge flank elevation, axial valley width, and long-wavelength axial depth, all correlate such that the segments become more dominated by tectonic spreading as the mean axial depth increases and melt flux decreases. From this we conclude that second-order segmentation of slow spreading mid-ocean ridges is largely driven by melt flux, which is, in turn, driven in part by underlying mantle temperature. This result is surprising given that sub-ridge upper-mantle is unlikely to preserve temperature variations for any significant duration of time (e.g., millions of years). Other than mantle temperature, another explanation of variations in melt supply may be mantle composition, such as volatile content or other fusible components enhancing melt supply, or major element depletion resulting in a more refractive mantle and a lower melt flux. For example, mantle relatively enriched in fusible components (i.e., more primitive and/or water-rich) can yield a greater melt fraction and more melt flux compared with a more depleted mantle composition under the same conditions of temperature, spreading rate and passive isentropic upwelling (Sleep, 1984; McKenzie and Bickle, 1988; Nichols et al., 2002; Ito and Mahoney, 2005). Exploring relationships between mantle composition and ridge structure could further test this hypothesis.

5. Summary and conclusions

We have made a global study of second-order segments from the major mid-ocean spreading-ridges and show that they correlate in length and frequency with spreading rate. Comparison between the slow-spreading CA and KA-MAR ridge segments shows that they both exhibit wide-ranges in second-order segment morphology. This is despite similar spreading rates, ridge depths and isolation from known mantle hot-spots. At the KA-MAR and CR, segment morphology varies with axial depth, ridge flank height and, to some extent, axial valley width. These parameters also vary with melt fraction and melt supply, showing that the morphology of slow spreading centres is extremely sensitive to variations in magma supply resulting from variation in the degree of mantle melting.

Acknowledgments

We would like to thank the officers and crew of the RRS Charles Darwin (Cruise 149) for their tenacity and professionalism, working through the SW monsoon season, and with the uncertain threat to the security of the vessel in these waters. We would like to thank Vikki Gunn for her help extracting the global ridge segmentation data and Tim LeBas for helping process the swath bathymetry data from the Carlsberg Ridge. We would like to dedicate this paper to the memory of our colleague and fellow Carlsberg Ridge voyager, Tina Hayes, who was cruelly taken at such a young age. The work was funded by a Natural Environment Research Council (NERC) grant to Murton.

References

Becker, J.J., Sandwell, D.T., Smith, W.H.F., Braud, J., Binder, B., Depner, J., Fabre, D., et al., 2009. Global bathymetry and elevation data at 30 arc seconds resolution: SRTM30_PLUS. *Mar. Geod.* 32, 355–371.

Buck, W.R., Lavier, L.L., Poliakov, A.N.B., 2005. Modes of faulting at mid-ocean ridges. *Nature* 434, 719–723.

Cann, J.R., Blackman, D.K., Smith, D.K., McAllister, E., Janssen, B., Mello, S., Avgerinos, E., Pascoe, A.R., Escartin, J., 1997. Corrugated slip surfaces formed at ridge-transform intersections on the Mid-Atlantic Ridge. *Nature* 385, 329–332.

Carbotte, S.M., Small, C., Donnelly, K., 2004. The influence of ridge migration on the magmatic segmentation of mid-ocean ridges. *Nature* 429, 743–745.

Chen, Y., Morgan, W.J., 1990. A nonlinear rheology model for mid-ocean ridge axis topography. *J. Geophys. Res.* 95, 17583–17604.

Cochran, J.R., Sempere, J.-C., 1997. SEIR Scientific Team. The southeast Indian Ridge between 88°E and 118°E : gravity anomalies and crustal accretion at intermediate spreading rates. *J. Geophys. Res.* 102, 15463–15487.

DeMets, C., Gordon, R., Argus, D.F., 2010. Geologically current plate motions. *Geophys. J. Int.* 181, 1–80.

Gale, A., Langmuir, C.H., Dalton, C.A., 2014. The global systematics of ocean ridge basalts and their origin. *J. Petrol.* 55, 1051–1082.

Gente, P., Pockalny, R.A., Durand, C., Deplus, C., Maia, M., Ceuleneer, G., Mével, C., Cannat, M., Laverne, C., 1995. Characteristics and evolution of the segmentation of the Mid-Atlantic Ridge between 20°N and 24°N during the last 10 million years. *Earth Planet. Sci. Lett.* 129, 55–71.

Griffiths, R.W., Fink, J.H., 1992a. Solidification and morphology of submarine lavas: a dependence on extrusion rate. *J. Geophys. Res.* Solid Earth 97, 19729–19737.

Griffiths, R.W., Fink, J.H., 1992b. The morphology of lava flows in planetary environments: predictions from analog experiments. *J. Geophys. Res.* Solid Earth 97, 19739–19748.

Head, J.W., Wilson, L., Smith, D.K., 1996. Mid-ocean ridge eruptive vent morphology and substructure: evidence for dike widths, eruption rates, and evolution of eruptions and axial volcanic ridges. *J. Geophys. Res.* 101, 28265–28280.

Hooft, E.E., Detrick, R.S., 1995. Relationship between axial morphology, crustal thickness, and mantle temperature along the Juan de Fuca and Gorda Ridges. *J. Geophys. Res.* Solid Earth 100, 22499–22508.

Ildefonse, B., Blackman, D.K., John, B.E., Ohara, Y., Miller, D.J., MacLeod, C.J., 2007. Oceanic core complexes and crustal accretion at slow-spreading ridges. *Geology* 35, 623–626.

Ito, G., Mahoney, J.J., 2005. Flow and melting of a heterogeneous mantle: 1. Method and importance to the geochemistry of ocean island and mid-ocean ridge basalts. *Earth Planet. Sci. Lett.* 230, 29–46.

Klein, E.M., Langmuir, C.H., 1987. Global correlations of ocean ridge basalt chemistry with axial depth and crustal thickness. *J. Geophys. Res.* 92, 8089–8115.

Lavier, L.L., Buck, W.R., Poliakov, A.N., 1999. Self-consistent rolling-hinge model for the evolution of large-offset low-angle normal faults. *Geology* 27, 1127–1130.

Lin, J., Phipps Morgan, J., 1992. The spreading rate dependence of three-dimensional mid-ocean ridge gravity structure. *Geophys. Res. Lett.* 19, 13–16.

Lin, J., Purdy, G.M., Schouten, H., Sempere, J.-C., Zervas, C., 1990. Evidence from gravity data for focussed magmatic accretion along the Mid-Atlantic Ridge. *Nature* 344, 627–632.

Macdonald, K.C., Fox, P.J., Perram, L.J., Eisen, M.F., Haymon, R.M., Miller, S.P., Carbotte, S.M., Cormier, M.H., Shor, A.N., 1988. A new view of the mid-ocean ridge from the behaviour of ridge-axis discontinuities. *Nature* 335, 217–225.

MacLeod, C.J., Searle, R.C., Murton, B.J., Casey, J.F., Mallows, C., Unsworth, S.C., Achenbach, K.L., Harris, M., 2009. Life cycle of oceanic core complexes. *Earth Planet. Sci. Lett.* 287, 333–344.

Magde, L.S., Sparks, D.W., 1997. Three-dimensional mantle upwelling, melt generation, and melt migration beneath segment slow spreading ridges. *J. Geophys. Res.* 102, 20571–20583.

McKenzie, D., Bickle, M.J., 1988. The volume and composition of melt generated by extension of the lithosphere. *J. Petrol.* 29, 625–679.

Mendel, V., Sauter, D., Rommevaux-Jestin, C., Patriat, P., Lefebvre, F., Parson, L.M., 2003. Magmato-tectonic cyclicity at the ultra-slow spreading Southwest Indian Ridge: evidence from variations of axial volcanic ridge morphology and abyssal hills pattern. *Geochem. Geophys. Geosyst.* 4 (5), 2003.

Murton, B.J., Parson, L.M., 1993. Segmentation, volcanism and deformation of oblique spreading centres: a quantitative study of the Reykjanes Ridge. *Tectonophysics* 222, 237–257.

Murton, B.J., Taylor, R.N., Thirlwall, M.F., 2002. Plume–ridge interaction: a geochemical perspective from the Reykjanes Ridge. *J. Petrol.*, 43, pp. 1987–2012.

Murton, B.J., Taylor, R.N., 2003. pp. Spreading-ridge geometry, hydrothermal activity, and the influence of modern and ancient hotspots on the Carlsberg Ridge—northwestern Indian Ocean. National Oceanography Centre, Southampton, UK p. 37, Cruise Report: CD149—RRS Charles Darwin 18th July to 6th August, 2003.

Murton, B.J., Baker, E.T., Sands, C.M., German, C.R., 2006. Detection of an unusually large hydrothermal event plume above the slow-spreading Carlsberg Ridge: NW Indian Ocean. *Geophys. Res. Lett.* 33, 1–5.

Nichols, R.L., Carroll, M.R., Höskuldsson, Á., 2002. Is the Iceland hot spot also wet? Evidence from the water contents of undegassed submarine and subglacial pillow basalts. *Earth Planet. Sci. Lett.* 202, 77–87.

Olive, J.A., Behn, M.D., Tucholke, B.E., 2010. The structure of oceanic core complexes controlled by the depth distribution of magma emplacement. *Nat. Geosci.* 3, 491–495.

Osmaston, M.F., 1971. Genesis of ocean ridge median valleys and continental rift valleys. *Tectonophysics* 11, 387–405.

Phipps Morgan, J., Parmentier, E.M., Lin, J., 1987. Mechanisms for the origin of mid-ocean ridge axial topography: implications for the thermal and mechanical structure of accreting plate boundaries. *J. Geophys. Res.* 92, 12823–12836.

Poore, H.R., White, N.J., Jones, S.M., 2009. A Neogene chronology of Iceland plume activity from V-shaped ridges. *Earth Planet. Sci. Lett.* 283, 1–13.

Purdy, G.M., Sempere, J.-C., Schouten, H., Dubois, D.L., Goldsmith, R., 1990. Bathymetry of the Mid-Atlantic Ridge, $24\text{--}31^\circ\text{N}$: a map series. *Mar. Geophys. Res.* 12, 247–252.

- Rona, P.A., 1976. Asymmetric fracture zones and seafloor spreading. *Earth Planet. Sci. Lett.* 30, 109–116.
- Rona, P.A., Gray, D.F., 1980. Structural behavior of fracture zones symmetric and asymmetric about a spreading axis: Mid-Atlantic Ridge crest (1at 23°N to 27°N). *Geol. Soc. Am. Bull.* 91, 485–496.
- Rabain, A., Cannat, M., Escartín, J., Pouliquen, G., Deplus, C., Rommevaux-Jestin, C., 2001. Focused volcanism and growth of a slow spreading segment (Mid-Atlantic Ridge, 35°N). *Earth Planet. Sci. Lett.* 185, 211–224.
- Schilling, J.G., Zajac, M., Evans, R., Johnston, T., White, W., Devine, J.D., Kingsley, R., 1983. Petrologic and geochemical variations along the Mid-Atlantic Ridge from 29 degrees N to 73 degrees North. *Am. J. Sci.* 283, 510–586.
- Schouten, H., Dick, H.J.B., Klitgord, K.D., 1987. Migration of mid-ocean-ridge volcanic segments. *Nature* 326, 835–839.
- Searle, R.C., Keeton, J.A., Owens, R.B., White, R.S., Mecklenburgh, R., Parsons, B., Lee, S.M., 1998. The Reykjanes Ridge: structure and tectonics of a hot-spot-influenced, slow-spreading ridge, from multibeam bathymetry, gravity and magnetic investigations. *Earth Planet. Sci. Lett.* 160, 463–478.
- Sempéré, J.C., Lin, J., Brown, H.S., Schouten, H., Purdy, G.M., 1993. Segmentation and morphotectonic variations along a slow-spreading center: the Mid-Atlantic Ridge (24 00' N–30 40' N). *Mar. Geophys. Res.* 15, 153–200.
- Sleep, N.H., 1984. Tapping of magmas from ubiquitous mantle heterogeneities: an alternative to mantle plumes? *J. Geophys. Res.* 89, 10029–10041.
- Smith, W.H.F., Sandwell, D.T., 1997. Global seafloor topography from satellite altimetry and ship depth soundings. *Science* 277, 1956–1962.
- Thibaud, R., Gente, P., Maia, M., 1998. A systematic analysis of the Mid-Atlantic Ridge morphology and gravity between 15°N and 40°N: constraints of the thermal structure. *J. Geophys. Res.* 103, 223–243.
- Thibaud, R., Dauteuil, O., Gente, P., 1999. Faulting pattern along slow-spreading ridge segments: a consequence of along-axis variation in lithospheric rheology. *Tectonophysics* 312, 157–174.
- Tivey, M.A., Tucholke, B.E., 1998. Magnetization of oceanic crust from 0 to 29 Ma formed at the Mid-Atlantic Ridge 25°30' to 27°10'N. *J. Geophys. Res.* 103, 17807–17826.
- Tucholke, B.E., Lin, J., 1994. A geological model for the structure of ridge segments in slow spreading ocean crust. *J. Geophys. Res.* 99, 11937–11958.
- Tucholke, B.E., Lin, J., Kleinrock, M.C., 1998. Megamullions and mullion structure defining oceanic metamorphic core complexes on the Mid-Atlantic Ridge. *J. Geophys. Res.* 103, 9857–9866.
- White, R.S., Brown, J., Smallwood, J.R., 1995. The temperature of the Iceland plume and origins of outward-propagating V-shaped ridges. *J. Geol. Soc.* 152, 1039–1045.